Cohesive zone modelling and the fracture process of structural tape

Stigh, Ulf; Biel, Anders; Svensson, Daniel

Published in:
Procedia Structural Integrity

Link to article, DOI:
10.1016/j.prostr.2016.06.031

Publication date:
2016

Document Version
Publisher's PDF, also known as Version of record

Available online at www.sciencedirect.com

ScienceDirect

Procedia Structural Integrity 2 (2016) 235–244

Structural Integrity Procedia

www.elsevier.com/locate/procedia

21st European Conference on Fracture, ECF21, 20-24 June 2016, Catania, Italy

Cohesive zone modelling and the fracture process of structural tape

Ulf Stigh[a*], Anders Biel[b], Daniel Svensson[a]

[a]*School of Engineering, University of Skövde, SE-541 28 Skövde, Sweden*
[b]*Department of Wind Energy, Technical University of Denmark, DK-4000 Roskilde, Denmark*

Abstract

Structural tapes provide comparable toughness as structural adhesives at orders of magnitude lower stresses. This is potentially useful to minimize the effects of differences in thermal expansion in the joining of mixed materials. The strength properties are modelled using the cohesive zone model. Thus, a cohesive zone represents the tape, i.e. stresses in the tape are transmitted to the substrates through tractions determined by the separations of the surfaces of substrates. This simplification allows for structural analysis of large complex structures. The relation between the traction and the separation is measured experimentally using methods based on the path independence of the *J*-integral. Repeated experiments are performed at quasi-static loading. A mixed mode cohesive law is adapted to the experimental data. The law is implemented as a UMAT in Abaqus. Simulations show minor thermal distortions due to thermal loading and substantial structural strength in mechanical loading of a mixed material structure.

Peer-review under responsibility of the Scientific Committee of ECF21.

Keywords: Mixed material joint; structural strength; FEA; J-integral method

1. Introduction

A key-technology for lightweight design and by that limiting our carbon footprint is the capability to join different materials. By mastering this, the optimal material can be chosen for each part of a structure. In the car

* Corresponding author. Tel.: +46-(0)500-448508.
E-mail address: ulf.stigh@his.se

Peer-review under responsibility of the Scientific Committee of ECF21.
10.1016/j.prostr.2016.06.031

industry, the challenge is to decrease the present allowed average of 130 grams/km of CO_2 to 95 grams/km in 2021. A conceivable method to achieve the goal is to combine advanced composite materials with high-strength metals.

One difficulty in mixed-material joining is the difference in thermal expansion properties. For instance, imagine that two sheets of different materials are joined. When the temperature changes stresses and shape distortions occur. The size depends on the stiffness of the joint between the two sheets; with higher stiffness larger stresses and more severe shape distortion develop. A class of acrylic foam pressure sensitive adhesive (PSA)† provides similar fracture toughness as structural adhesives but at low stress and stiffness. The low stiffness gives smaller stresses and shape distortion than a conventional adhesive would give in a mixed material joint. PSA is today used to e.g. mount windows on buildings and to join exterior components on vehicles. However, to exploit the full potential, methods to predict the strength of structures joined with PSA need to be developed. Modern competitive product development methods rely on the ability to simulate. To this end, we suggest the use of cohesive layer (CL) modelling.

The CL model has previously been exploited with good results for stiffer adhesive joints, cf. e.g. Yang and Thouless (2001). With this model, the tape is characterized by a cohesive zone transmitting traction from one adherend to the other. The size and orientation of the traction vector depend on the deformation of the tape between the two adherends. Figure 1 illustrates the basic deformation modes considered in a 2D setting. In 3D, two orthogonal shear components are considered. Thus, the normal component of the traction vector is σ and the in-plane components are τ_1 and τ_2, the conjugated deformation measures are w, v_1 and v_2, respectively. Provided only one of the deformation modes are active, notation from fracture mechanics is borrowed. Thus, mode I loading acts if σ and w dominate, and mode II and III if τ and v dominate.

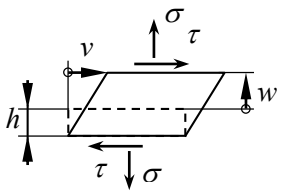

Fig. 1. Deformation modes of the tape with thickness h: peel, w, and shear, v. Conjugated stress components σ and τ.

Several cohesive laws are suggested in the literature, cf. e.g. McGarry et al. (2014). A cohesive law provides the relation between the separation of the prospective crack surfaces of the adherends and the traction. In monotonically increasing deformation, as may be anticipated in e.g. a strength analysis, the cohesive law is given by a set of functions $\sigma(w,v_1,v_2)$, $\tau_1(w,v_1,v_2)$, and $\tau_2(w,v_1,v_2)$, i.e. for each set of (w,v_1,v_2) one and only one set of (σ,τ_1,τ_2) corresponds. These relations can either be based on a potential ϕ, e.g. $\sigma=\partial\phi/\partial w$ or be non-potential based, cf. Svensson et al. (2016). In order to treat more general loading, plasticity and damage are often used to model the inelasticity, cf. e.g. Biel and Stigh (2010).

By the CL-model, we neglect effects of the deformation of the material in the neighborhood of the material line connecting corresponding points on the upper and lower adherend. This appears to be a valid simplification if the adherends are much stiffer than the tape and if the gradients, in the plane of the tape, are small. It may be noted that this model also results from asymptotic analyses in linear elasticity, cf. e.g. Schmidt (2008).

Cohesive laws for pure mode loading of the present PSA are measured and reported by Biel at al. (2014) and by Biel and Svensson (2016). The next section gives a recapitulation of the methods and results together with an extension to mixed mode loading. After this, a simulation model is set-up and used to evaluate the behavior of a mixed-material joint. The paper ends with a discussion and some conclusions.

† Also known as pressure sensitive tape

2. Measured cohesive laws for PSA

Two methods are developed to measure the cohesive law for PSA; one for mode I loading and one for mode III loading. Both methods are based on the Double Cantilever Beam (DCB) specimen geometry, cf. Fig. 2. The tape with thickness h resides on the x-z-plane. It is severely loaded at its start ($x = 0$) and in mode I loading the elongation is w at the edge. In mode III, the shear is v at the edge. The far end of the specimen, i.e. at $x = l - a$ is virtually unloaded.

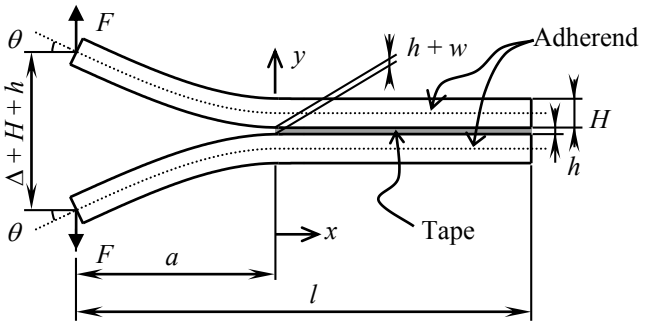

Fig. 2. Double Cantilever Beam specimen with PSA with thickness h and out-of-plane width b; corresponding width of specimen is B.

Utilizing the path independent J-integral, the rate at which energy is captured at the start of the tape is alternatively written

$$J \equiv \int_S \left(W n_x - \sigma_{ik} u_{i,x} n_k \right) \mathrm{d}S = \frac{2F \sin\theta}{b} = \int_0^w \sigma\left(\tilde{w}\right) \mathrm{d}\tilde{w} \tag{1}$$

Index notation is utilized where the subscript indicates the coordinate, a comma indicates differentiation, and summation should be taken over repeated indexes. The first integral is the definition of the J-integral, cf. Rice (1968). This gives the energy per unit area in the x-z-plane provided the integration path S, starting at a point just below the start of the tape and extending counterclockwise to a point just above the start of the tape is shrunk to a vertical path. In that case, the traction $\sigma_{ik} n_k$ in the second term of the integrand is zero by the boundary condition. Thus, only the integral of the strain energy density W through the thickness remains. This shows that the integral equals the captured energy per unit area at the start of the tape. By changing variable in the resulting integral, the consumed area below the cohesive law, as shown in the last expression results. The notation $\tilde{w}$ is used to distinguish between the dummy variable in the integrand and the upper boundary of the integral. The deformation of the tape at $x = 0$ is denoted w in this integral, cf. Fig. 2. Now, if all material of the specimen can be considered to be governed by a strain energy density – different in the adherend and in the tape, but the same functions for all x – then the integral is path independent and the second equality holds. This is shown by extending S to a path following the external boundary of the specimen, cf. Nilsson (2006). The rotation[‡] $\theta = -u_{y,x}$ where u_y is the y-components of the displacement vector and B is the out-of-plane width of the specimen. In this expression, we have assumed that the specimen is long enough to secure that the far right boundary of the specimen is stress free, cf. Fig. 2.

[‡] The minus sign holds for the upper adherend, a plus sign should replace this for the lower adherend.

A differentiation of the last equality in Eq. (1) yields

$$\sigma(w)=\frac{2}{b}\frac{\partial(F\sin\theta)}{\partial w} \tag{2}$$

Thus, by measuring F, θ and w during an experiment with monotonically increasing Δ, the cohesive law is given by Eq. (2). It should be noted that we assume that the same cohesive law governs all of the tape and that w is measured at the start of the tape, cf. Fig. 2. The method is utilized in several studies. An overview is given in Stigh et al. (2010). In mode III, σ is replaced with τ and w with v, cf. Biel and Svensson (2016) and section 2.2 below.

The PSA is 3M VHB-4611F. This is an acrylic foam tape with a nominal thickness h = 1.1 mm. All tests are performed at room temperature.

2.1. Mode I

Biel et al. (2014) report data for mode I loading. Nominal dimensions for the specimen are H = 5 mm, l = 1 m, a = 0.1 m, b = 19 mm and B = 30 mm. Before joining the specimens, the surfaces of the steel adherends are cleaned with heptane and acetone. The time between the manufacturing of the specimens and the experiment is more than 100 hours. Figure 3 shows a specimen in the test machine.

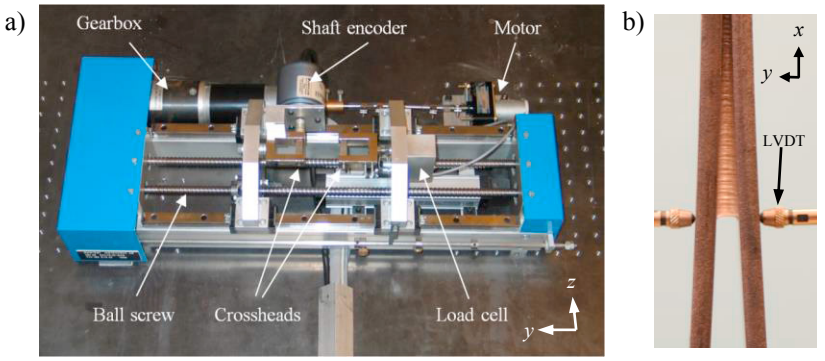

Fig. 3. (a) Test machine without specimen; (b) mounted and loaded specimen (from Biel et al., 2014).

The test machine (Swetest 100-168) loads the specimen through crossheads with ball bearings to minimize any introduction of bending moments induced in the specimen by friction. The rotation θ is measured with a shaft encoder with $2 \cdot 10^5$ pulses per revolution and a load cell with 500 N capacity measures F. The deformation w of the tape is measured with LVDTs, cf. Fig. 3b. All experiments are conducted quasistatically; the loading points separate symmetrically with a fixed rate $\dot{\Delta}$ = 30 μm/s. Figure 4a shows J vs. w and Fig. 4b σ vs. w. A novelty is the appearance of two stress peaks in the cohesive law; the first is at about 0.35 MPa and the second at about 0.55 MPa. Similar peaks are shown for another PSA by Biel and Stigh (2016). It is noted that the stresses are small and the influence of the ambient pressure is important for applications where the pressure is substantially different from the normal air pressure of about 0.1 MPa. Final fracture occurs at an engineering strain of about 5. The fracture energy in mode I J_{Ic}, is about 2 kN/m.

2.2. Mode III

Biel and Svensson (2016) report the cohesive law in shear for PSA 3M VHB-4611F. A modified DCB-specimen configuration is used, cf. Fig. 5. It is denoted the Split Cantilever Beam (SCB) specimen. The basic idea is to load the beams through their shear centers, cf. e.g. Beer et al. (2006). By this, the beams essentially translate in the x-y-

plane without rotating around the x-axis. Thus, the tape suffers almost pure shear loading. This is confirmed in Biel and Svensson (2016) through FE-simulations.

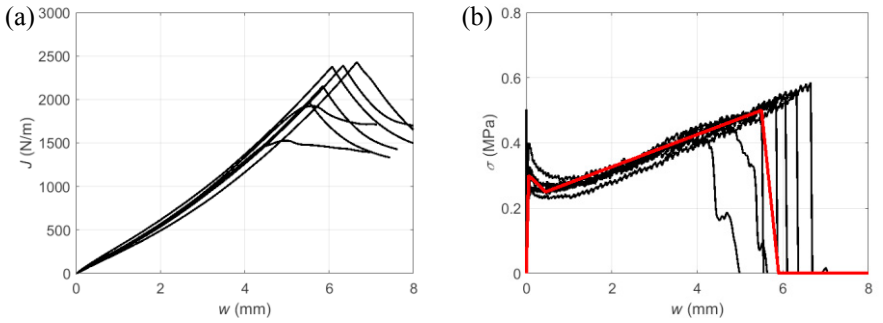

Fig. 4. Measured data mode I, black curves (a) J vs. w; (b) cohesive law (Biel et al. 2014). Red curve is an adaption for FE-simulations.

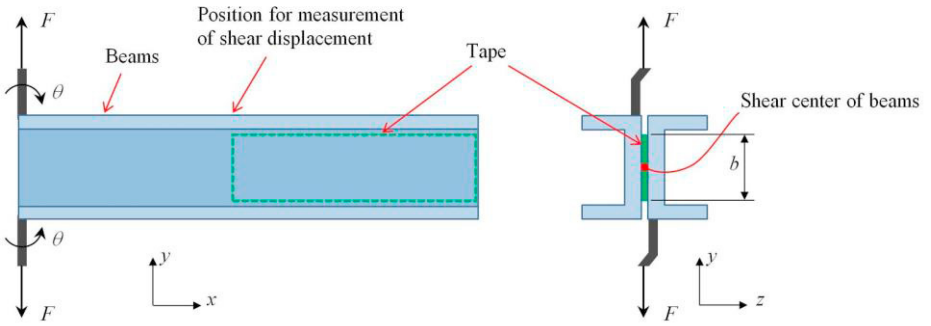

Fig. 5. SCB-specimen in two perspectives. *Left*: x-y-plane; *Right*: (b) y-z-plane.

The basic geometry of the specimen is l = 2 m and a = 0.2 m. The width of the tape is b = 19 mm, cf. Fig. 5, the details are given by Biel and Svensson (2016). The adherends are made of extruded aluminum. After cleaning the surfaces the joint is assembled. The time between the manufacturing of the specimens and the experiment is more than the recommended 72 hours.

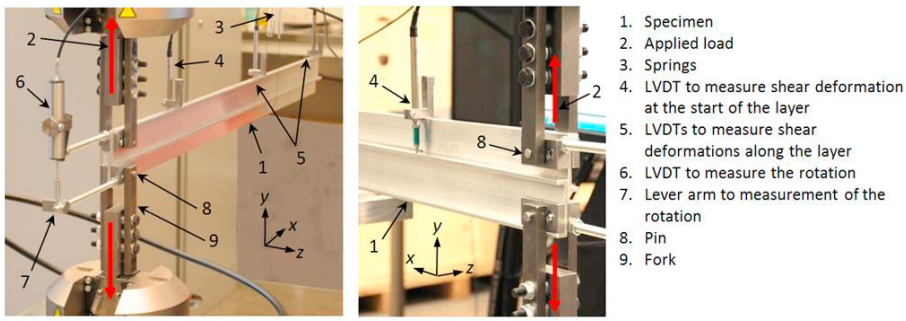

Fig. 6. Experimental configuration from two perspectives (Biel and Svensson, 2016).

The experiments are performed in a servo hydraulic test machine (Instron 8800) at the constant loading rate $\dot{\Delta}=2$ mm/s, cf. Fig. 6. This is larger than for the mode I experiments. However, the difference in specimen geometry partly compensates for this difference leading to comparable strain rates in the tape in the mode I and III experiments. An LVDT is used to measure v at the start of the tape, cf. #4 in Fig. 6; the rotation θ is measured using LVDT at a 180 mm long extension of the specimen (#6) and Δ as measured internally in the test machine at the point of load application.

Figure 7 shows J vs. v and τ vs. v as evaluated from Eqs. (1) and (2), respectively. The shear stress increases almost linearly to a maximum at about 0.5 MPa at a shear deformation of about 8 mm. After a plateau, the stress then drops to zero and the formation of a crack at about $v = 9$ mm. Thus, final fracture occurs at an engineering strain of about 8. The fracture energy in mode III J_{IIIc}, is about 2.5 kN/m. Thus, comparable with the value in mode I.

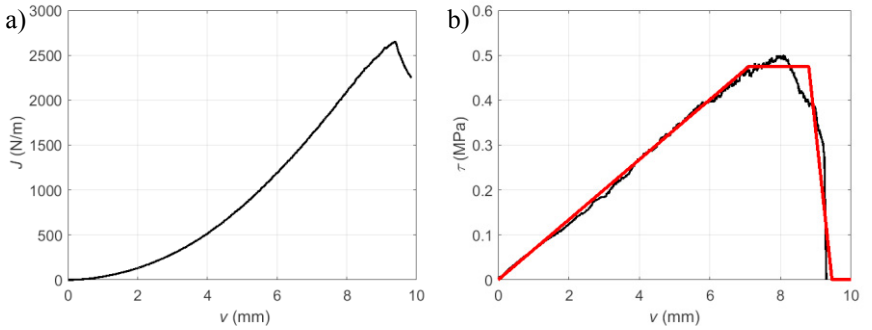

Fig. 7. Measured data mode III, black curves (a) J vs. v; (b) cohesive law (Biel and Svensson, 2016). Red curve is an adaption for FE-simulations.

2.3. Mixed mode model and data

In this section, the Yang and Thouless (2001) mixed mode model is introduced in a rate form and the present experimental data are used to set the parameters of the model.

The total rate at which energy per unit area is captured in the tape is given by

$$\dot{\phi} = \dot{\phi}_{\mathrm{peel}} + \dot{\phi}_{\mathrm{shear}} \tag{3}$$

where a dot represents a strictly increasing time-like variable, and where

$$\dot{\phi}_{\mathrm{peel}} = \begin{cases} \sigma\left(w_{\max}\right)\dot{w} \text{ if } \left(w - w_{\max}\right)\dot{w} > 0 \\ 0 \text{ otherwise} \end{cases}; \qquad \dot{\phi}_{\mathrm{shear}} = \begin{cases} \tau\left(v_{\max}\right)\dot{v} \text{ if } \left(v - v_{\max}\right)\dot{v} > 0 \\ 0 \text{ otherwise} \end{cases}, \tag{4}$$

with

$$\dot{v} \equiv \sqrt{\dot{v}_1^2 + \dot{v}_2^2}; \qquad w_{\max} = \sup\left(w\right); \quad v_{\max} = \sup\left(v\right). \tag{5}$$

The notation sup indicates the largest value of the variable encountered during the loading history. It is noted that ϕ_{peel} and ϕ_{shear} at the start of the tape in the pure mode loadings above equal J_{I} and J_{III}, respectively. The relations $\sigma(w_{\max})$ and $\tau(v_{\max})$ are adaptions of sequences of linear segments to the experimental measured $\sigma(w)$ and $\tau(v)$ data, cf. the red curves in Figs. 4b and 7b. In this adaption, three features are of special importance for structural strength, *viz*. the maximum stress, the maximum deformation before fracture, and the fracture energy, i.e. the complete area

below the cohesive law. The stress components are given by

$$\sigma = \begin{cases} \sigma\left(w_{\max}\right) \text{ if } \left(w - w_{\max}\right)\dot{w} > 0 \\ \dfrac{w}{w_{\max}}\sigma\left(w_{\max}\right) \text{ otherwise} \end{cases} ; \qquad \tau = \begin{cases} \tau\left(v_{\max}\right) \text{ if } \left(v - v_{\max}\right)\dot{v} > 0 \\ \dfrac{v}{v_{\max}}\tau\left(v_{\max}\right) \text{ otherwise} \end{cases} . \tag{6}$$

Thus, unloading is assumed linear elastically with no remaining deformation after a complete unloading. The shear stress vector is set to be co-linear with the shear deformation vector, i.e.

$$\tau_1 = \tau\frac{v_1}{v}; \qquad \tau_2 = \tau\frac{v_2}{v} . \tag{7}$$

In line with the original Yang and Thouless' model, the peel and shear components are, up to this point, treated independently of each other. The coupling is given by the life fraction

$$D = \frac{\phi_{\text{peel}}}{J_{\text{Ic}}} + \frac{\phi_{\text{shear}}}{J_{\text{IIIc}}} . \tag{8}$$

Thus, $D = 0$ for the virgin tape and when $D = 1$, the tape is locally fractured. Thus, in pure mode loading, fracture occurs at the anticipated fracture energies and no stresses appear in the other mode. As indicated, the shear properties in mode II and III are assumed to be equivalent.

The adapted, pure mode, cohesive laws are shown as red curves in Figs. 4b and 7b. For peel, the first stress peak is at 0.30 MPa and 0.055 mm. This corresponds to the stiffness $K_{\text{n}} = 5.5$ N/mm^3. The stress then decreases to 0.25 MPa at 0.45 mm. It then increases to a second stress peak at 0.50 MPa and 5.50 mm, and finally decreases to zero at 5.90 mm. This yields the fracture energy $J_{\text{Ic}} = 2.11$ kN/m, cf. the red curve in Fig. 4b. For shear, the stress first increases linearly with a sloop $K_{\text{t}} = 0.066$ N/mm^3 to 0.475 MPa at about 7.2 mm, then the stress remains constant to about 8.9 mm, it the decreases to zero at 9.4 mm to yield the fracture energy $J_{\text{IIIc}} = 2.635$ kN/m.

3. Example

A bi-material joint is studied where a bottom plate of steel is joined to a hat profile of an aluminum alloy using the present tape, cf. Fig. 8. The geometry is given by $t = 1.0$ mm, $R = 4$ mm, $c = 23$ mm, $g = 26$ mm, $d = 96$ mm, for notation cf. Fig. 8b. The distance between the supports is 350 mm and the total length is 500 mm. Supports and loading is symmetric. Both metals are considered elastic-plastic with linear, von Mises isotropic hardening. Material data are given in Table 1.

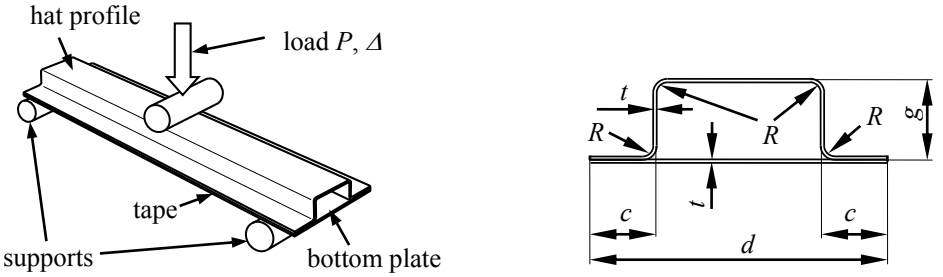

Fig. 8. Bi-material joint adapted from Carlberger et al. (2010).

Table 1. Material data for metals.

Metal	Young's modulus [GPa]	Poisson's ratio [-]	Coefficient of thermal expansion [10^{-6} °C^{-1}]	Yield strength [MPa]	Plastic hardening $\partial\sigma_Y^{eff}/\partial\varepsilon_{eff}^P$ [GPa]
Steel	200	0.300	11.0	550	1.05
Aluminum alloy	70.0	0.300	23.0	275	1.20

The FE-model is set-up in Abaqus version 6.11 using four node shell elements with reduced integration (S4R) and eight node cohesive elements COH3D8; the shell elements are modeled with shell offset to provide the correct coupling between the rotational degrees of freedom of the shell elements to the shear deformation of the cohesive elements, cf. e.g. Carlberger et al. (2008). Typical element sizes are 1 mm. Supports and loading roller are modeled as rigid contacts with the radius 50 mm with a friction coefficient 0.05. This version of Yang-Thouless' cohesive model is implemented as a user material (UMAT) in Abaqus.

Two load cases are considered. Load case A: A transversal prescribed displacement enforced on the upper roller as indicated in Fig. 8a; and Load case B: A uniform increase in temperature with increasing ΔT. The implicit solver is used in Abaqus using non-linear geometry.

3.1. Load case A: Mechanical load

The loading roller is displaced to the total displacement Δ = 70 mm as indicated in Fig. 8. This is done incrementally in about 200 load steps. No stabilization is utilized in the implicit FE-simulations. Abaqus default criteria for equilibrium is used and a maximum of 12 and typically 4 iterations are used to achieve equilibrium in each step. Figure 9a shows load vs. displacement of the loading cylinder. The load increases to a maximum of about 2.4 kN. Figure 9b shows a deformed geometry with the scale factor one and the effective stresses according to von Mises. Although very small stresses develop in the tape, substantial stresses develop in the metal parts. Although substantially deformed, no crack develops in the tape due to its considerable ductility. Figure 9c shows the deformed tape at the final load step and the field of life fraction D, cf. eq. (8). The life fraction D is smaller than 0.27 with a maximum in the section with the loading cylinder; note that D = 1 corresponds to fracture. Some unloading occurs during the final phases of the loading at this section. The loading capacity is limited by buckling and plasticity of the metal parts.

3.2. Load case B: Thermal load

In this load case the rollers are excluded from the model and one symmetrically located node on the hat profile is constrained from displacing and rotating. This constrain does not introduce any reaction forces or moments during thermal loading. The temperature is increased 60°C corresponding to an assembly of the joint at room temperature and a maximum use of the joint at 80°C. The solution is thermoelastic and no nonlinearity is activated in either metal or tape. Consequently only one load step is used and no iterations are needed to find equilibrium. Figure 10a shows the deformed geometry with the scale factor one and the displacement in the transversal direction. The maximum thermal distortion is smaller than 0.07 mm and the deformation is symmetric, as expected. Figure 10b shows the same geometry with the scale factor 300 and the von Mises' stress. As expected, the structure is slightly banana shaped with very small stresses induced by the thermal mismatch; the maximum stress is 1.25 MPa. Figure 10c shows the deformation of the tape $\sqrt{w^2+v_1^2+v_2^2}$. The maximum loading occurs at the ends of the tape and is smaller than 0.18 mm and is dominated by shear deformation. Thus, the analysis indicates no risk for fracture due to thermal loading.

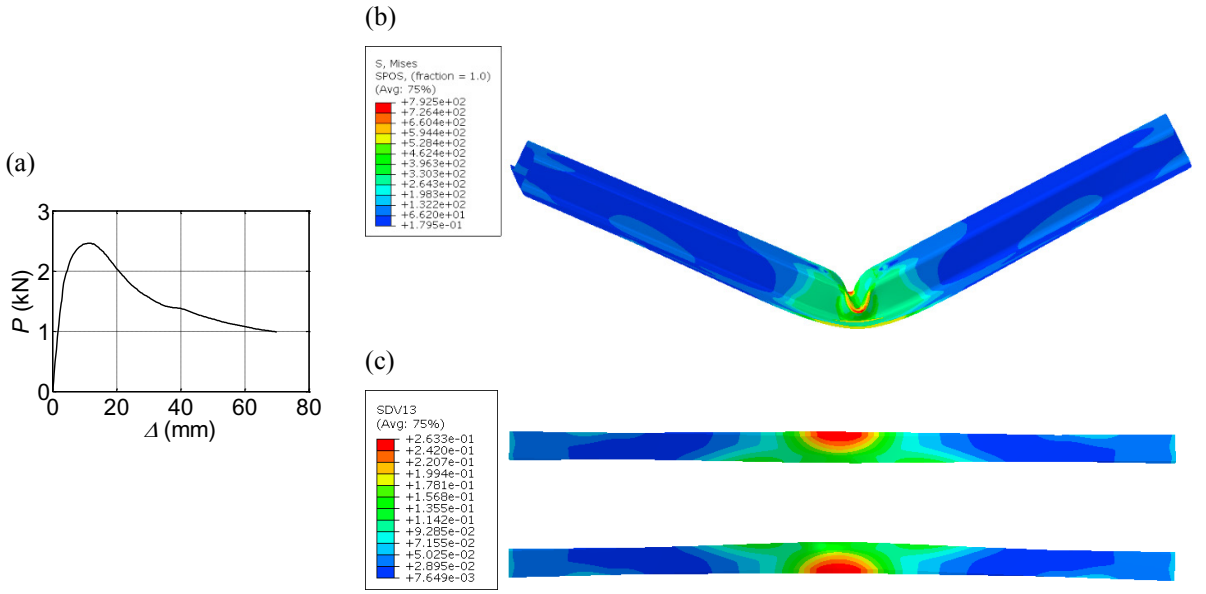

Fig. 9. Load case A: Mechanical load. (a) Load vs. displacement in the loading direction; (b) Deformed geometry with von Mises' effective stresses [MPa], with scale factor one; (c) Life fraction D in the isolated deformed tape viewed from above.

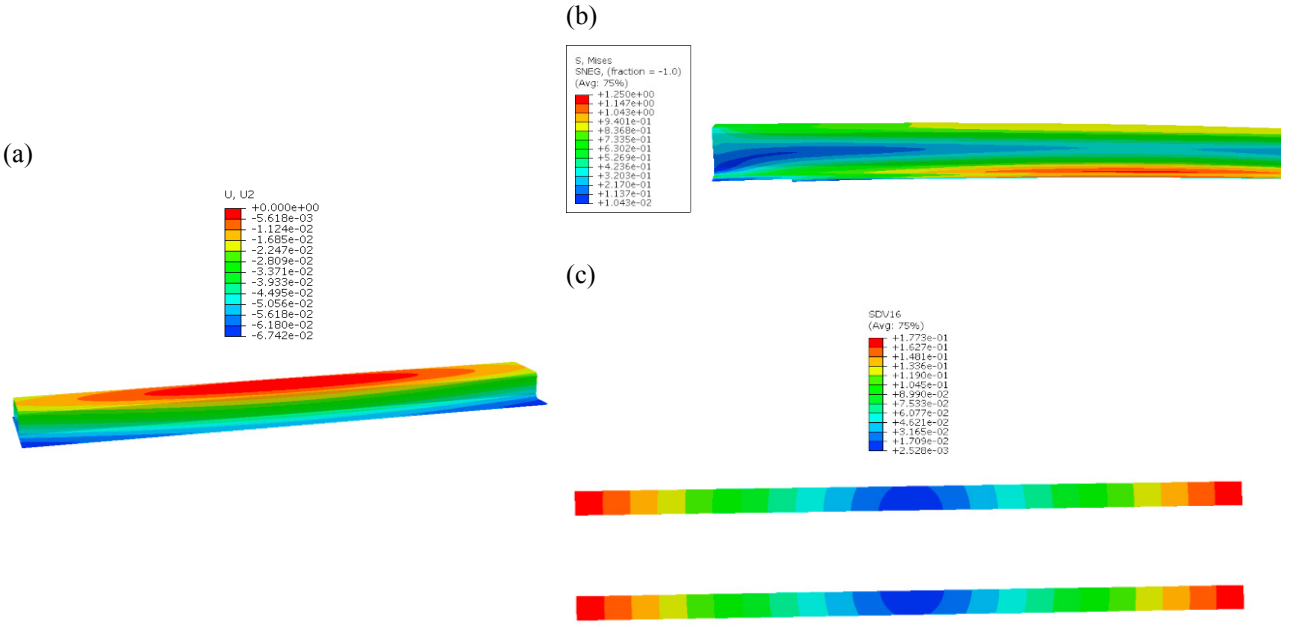

Fig. 10. Load case B: Thermal load. (a) Deformed geometry with scale factor one and size of displacement; (b) Deformed geometry with scale factor 300 and von Mises' stress [MPa]; (c) Isolated tape in deformed geometry with total deformation of tape $\sqrt{w^2+v_1^2+v_2^2}$

4. Discussion and conclusions

An integrated method to measure the properties of a PSA, to use these data to determine the parameters of a cohesive law, and finally implement the model and simulate the strength of a mixed material joint bonded with the PSA has been presented. The starting point is the CL model of the tape. With this, some details of the local fields of stress and strain are ignored in favor of the ability to simulate large and complex structures. Based on this model, two experimental methods are developed that provides the cohesive law corresponding to monotonically increasing load in mode I and III, respectively. The corresponding cohesive laws are measured for the PSA. In order to achieve a cohesive law capable of predicting the strength of large complex structures, the Yang-Thouless' cohesive law is used. At present, no experiments have been conducted to validate this model for tapes in mixed mode loading and unloading. The implementation as a UMAT in Abaqus is relatively unproblematic and the numerical performance is good demanding relatively few iterations to find equilibrium even at severe stages of loading. Some studies indicate that it is the plasticity and buckling of the metal shells that are the most demanding for the numerical method.

Experiments show that PSAs are able to take up large deformations before breaking. Although the stresses in the present PSA are small, the large ductility makes it very tough. These properties are interesting for mixed material joining where the ability to handle thermal loading is critical. With normal joining methods where high stiffness is often considered beneficial, a mixed material joint is often distorted to an unacceptable degree due to thermal mismatch. The joint may even break due to thermal loading. As demonstrated in load case 2, the flexibility of the PSA introduces only minor thermal distortions in a steel/aluminum joint of typical dimensions considered in the car industry. Moreover, the loading of the tape is also small. Load case 1 shows that although the stresses in the tape are small, the build-up structure is strong. Even after severe deformation, the tape is far from cracking. Thus, PSAs appear to possess interesting properties for mixed material joining. It should be stressed that this conclusion is drawn from a simulation result without accompanying experimental proof. At present, further studies on influences of e.g. temperature and loading rate are needed to give confidence in the results. Most importantly, the results need to be compared to experimental studies on complex structures.

Acknowledgements

The authors are grateful for financial support from ÅForsk and for material supported by 3M.

References

Beer, F.P., Johnston Jr, E.R., DeWolf, J.T., 2006. Mechanics of Materials. McGrew Hill Boston.

Biel, A., Alfredsson, K.S., Carlberger, T., 2014. Adhesive tapes; cohesive laws for a soft layer. Procedia Materials 3, 1389-1393.

Biel, A., Stigh, U., 2010. Damage and plasticity in adhesive layer - an experimental study. International Journal of Fracture, 165, 93–103.

Biel, A., Svensson, D., 2016. An experimental method to measure the shear properties of a flexible adhesive layer. In preparation.

Carlberger, T., Alfredsson, K.S., Stigh, U., 2008. Explicit FE-formulation of Interphase Elements for Adhesive Joints. International Journal for Computational Methods in Engineering Science & Mechanics 9, 288-299.

McGarry, J.P., Máirtín, É.Ó., Parry, G., Beltz, G.E., 2014. Potential-based and non-potential-based cohesive zone formulations under mixed-mode separation and over-closure – Part I: Theoretical analysis. Journal of the Mechanics and Physics of Solids 63, 336–362.

Nilsson, F., 2006. Large Displacement Aspects on Fracture Testing with Double Cantilever Beam Specimens. International Journal of Fracture 139, 305-311.

Rice, J.R., 1968. A path independent integral and the approximate analysis of strain concentration by notches and cracks. ASME Journal of Applied Mechanics, 35, 379-386.

Schmidt, P., 2008. Modelling of adhesively bonded joints by an asymptotic method. International Journal of Engineering Science 46, 1291-1324.

Stigh, U., Alfredsson, K.S., Andersson, T., Biel, A, Carlberger, T., Salomonsson, K., 2010. Some aspects of cohesive models and modelling with special application to strength of adhesive layers. International Journal of Fracture 165, 149-162.

Svensson, D., Alfredsson, K.S., Stigh, U., 2016. On the ability of coupled mixed mode cohesive laws to conform to LEFM for cracks in homogeneous orthotropic solids. In review.

Zhang, L., Wang, J., 2009. A generalized cohesive zone model of the peel test for pressure-sensitive adhesives. International Journal of Adhesion & Adhesives 29, 217-224.

Yang Q.D., Thouless M.D., 2001. Mixed-mode fracture analyses of plastically-deforming adhesive joints. International Journal of Fracture 110, 175–187.